NeuroImage: Clinical 4 (2014) 765–778

Contents lists available at ScienceDirect

NeuroImage: Clinical

journal homepage: www.elsevier.com/locate/ynicl

Modified human contrast sensitivity function based phase mask for susceptibility-weighted imaging

Wei-Hsin Wang[a], David C. Reutens[a], Zhengyi Yang[b], Giang Nguyen[a], Viktor Vegh[a,*]

[a] Centre for Advanced Imaging, University of Queensland, Australia
[b] School of Information Technology and Electrical Engineering, University of Queensland, Australia

ARTICLE INFO

Article history:
Received 20 December 2013
Received in revised form 22 March 2014
Accepted 28 April 2014

Keywords:
Susceptibility weighted imaging
Phase mask
Phase filtering
Human contrast sensitivity function

ABSTRACT

The aim of the work is to increase the visual information in magnetic resonance imaging based susceptibility weighted images. Our approach is to amplify spatial frequency information of the phase mask used to increase susceptibility weighting using a modified version of the human contrast sensitivity function. Thereby, we propose a modified version of the human contrast sensitivity function for use in phase mask creation. Comparison with conventional susceptibility-weighted imaging was undertaken on a qualitative basis and quantitatively with a number of established image quality metrics on *ex vivo* mouse brain magnetic resonance images obtained at 16.4 T at various echo times. Four experts also compared the quality of *in vivo* 1.5 and 3 T human brain magnetic resonance images generated with traditional susceptibility weighted imaging and with the new method. We found that parameters of the modified human contrast sensitivity function can be chosen to improve delineation of structural detail of mouse and human brains. Information contained in susceptibility-weighted images generated using the modified human contrast sensitivity function based phase mask corresponds to that in the conventional method, however the visual range over which it is depicted has improved visual perception. Hence, qualitative evaluation of information contained in susceptibility-weighted images can be improved by amplifying spatial frequencies where human contrast sensitivity is reduced.

1. Introduction

Magnetic resonance imaging (MRI) signals have magnitude and phase which may provide complementary information. Clinical diagnostic imaging most commonly relies on information based on signal magnitude, which is dominated by proton density and the influences of T_1 and T_2^* relaxation times. Signal phase also contains information about the structural properties of tissue with contrast arising from changes in the magnetic field induced by variations in magnetic susceptibility (Barnes and Haacke, 2012; Deistung et al., 2008; Duyn et al., 2007b; Haacke et al., 2004b). This effect scales with the static field strength of the scanner, and contrast differences in 7*T* phase images are sufficient to enable cortical structure to be distinguished in fine detail (Duyn et al., 2007b). The combination of both signal magnitude and phase are increasingly performed across a range of MRI studies (e.g. Beauchamp et al., 2011; de Champfleur et al., 2011; Jagadeesan et al., 2011; Zivadinov et al., 2012).

In susceptibility-weighted imaging (SWI), a phase mask derived from gradient recalled echo (GRE) MRI phase images is multiplied with the magnitude image (Barnes and Haacke, 2012; Deistung et al., 2008; Haacke et al., 2004b; Haacke et al., 2009). SWI has been used in cortical parcellation and in studying brain iron levels and calcification and blood oxygenation of the cerebral venous system (Barnes and Haacke, 2012; Deistung et al., 2008; Duyn, 2010; Haacke et al., 2004b; Haacke et al., 2005; Haacke and Ye, 2012; Robinson and Bhuta, 2011).

The distribution of voxel values achieved in SWI can be altered by changing the echo time of the GRE-MRI sequence, by changing the level of phase filtering prior to phase mask creation or by altering phase mask contrast by raising voxel values to a different power. A change in echo time requires additional data acquisition, whereas the latter two image processing techniques can be applied on already acquired data. Increased echo time leads to increased signal phase but also increases noise and signal magnitude decay. The exponentially decaying modulation of the signal magnitude with time imposes the condition that echo time should not be greater than T_2^* to maximize image contrast and to preserve detail (Duyn et al., 2007a; Vegh et al., 2012).

Phase masks may accentuate either negative and positive phase effects (Haacke et al., 2009; Mittal et al., 2009). Masks are made up

* Corresponding author at: Centre for Advanced Imaging, University of Queensland, St Lucia 4072, Australia.
E-mail address: v.vegh@uq.edu.au (V. Vegh).

2213-1582/$ - see front matter
http://dx.doi.org/10.1016/j.nicl.2014.04.012

of values between 0 and 1, with most values falling around 1. The power to which phase mask entries are raised alters the distribution of values. For example, if adjacent voxels in the phase mask have values of 0.9 and 0.909 (1% larger), raising voxel values to the power of 4 amplifies the difference to 4% ($0.9^4 = 0.6561$ versus $0.909^4 = 0.6827$). Hence, the distribution of voxel values changes with the power applied to the phase mask. Notably, the use of large powers leads to values concentrated around zero, diminishing the utility of the technique. Simulation studies have shown that contrast due to veins is maximized when a power between 3 and 5 is applied to the phase mask (Haacke et al., 2004b). Subsequently, the power of 4 has been employed in qualitative studies (Barnes and Haacke, 2012; Haacke et al., 2004b).

Our work focuses on changing the distribution of values in the phase mask to enhance SWI contrast. In human visual perception, contrast sensitivity varies with the spatial frequency of visual stimuli and if the latter is too high, the pattern of stimuli can no longer be perceived. For example, for an image consisting of vertical black and white stripes, if the stripes are very thin individual stripes cannot be distinguished and all that is seen is a gray image. If the width of the stripes is progressively increased, there is a threshold width above which stripes are perceptible. The relationship between visual contrast sensitivity and spatial frequency of visual stimuli is described by the Human Contrast Sensitivity Function (HCSF) (Farrell, 1999; Kelly, 1975; Mannos and Sakrison, 1974) (see Fig. 1(a)) and has been attributed to the eye's optical properties, cone photoreceptor sampling aperture and both passive and active neuronal connections (Daly, 1992). In addition to the spatial frequency of image components, the size of the image, its eccentricity and the level of background noise may also affect perception. Taking into account the HCSF, we sought to enhance the perception of image contrast across the spectrum of spatial frequencies by increasing contrast at spatial frequencies where contrast sensitivity is low. Fig. 1(b–d) provides a simple illustration of how perception of image content can be enhanced by applying a one-to-one mapping between the original image value and a new image with elevated contrast using a contrast sensitivity function. We developed a method of combining band-pass filtered phase images to amplify information in the low sensitivity region of the HCSF spectrum, resulting in a novel approach of creating phase masks which were multiplied with the magnitude image to generate a new SWI image. We evaluated the performance of the method across a range of echo times and parameter settings. HCSF-modified SWI results were qualitatively and quantitatively compared with traditional SWI reconstructions.

2. Experimental

2.1. MRI data acquisition — 16.4 T ex vivo mouse brain

MRI raw data were acquired on a 16.4 T Bruker Biospin® animal MRI instrument running Paravision® (V5). An *ex vivo* mouse brain was imaged with the standard gradient recalled echo (GRE) sequence. The imaging acquisition parameters applied were: matrix size = 256 × 256, repetition time (TR) = 1.5 s, flip angle (α) = 30°, bandwidth = 50,000 Hz, field-of-view (FOV) = 10.2 mm × 10.2 mm, slice thickness and separation = 0.5 mm and number of slices = 20. Zero filling was not applied. Multiple echo times (T_E) were set to obtain different T_2^*-weighting levels in resultant images. The range of T_E selected is from 3.5 to 58.5 ms, in steps of 5 ms. The T_2^*-relaxation time of the mouse brain was calculated through the standard Paravision relaxometry sequence, which was 24 ms. The filtering of raw data beyond what is standard in Paravision was not performed.

2.2. MRI data acquisition — 1.5 and 3 T in vivo human brain

The research was approved by the hospital's Human Research Ethics Committee. Forty-three patients admitted with a clinical diagnosis of acute ischemic stroke to Royal Brisbane and Women's Hospital were recruited between May 2011 and April 2012. Patients underwent an MRI examination at admission from which five MRI data sets were randomly selected for this study. MRI susceptibility weighted images were acquired on a 1.5 T Siemens® Avanto and 3 T Siemens® Trio human scanners running Syngo® housed at the hospital. The Syngo SWI sequence was used with the following parameters: matrix size = 224 × 256, repetition time (TR) = 200 ms, echo time (TE) = 20 ms, flip angle = 15°, bandwidth = 120 Hz per pixel, in-plane resolution = 1 mm × 1 mm, slice thickness and separation = 2 mm and number of slices = 72.

3. Theory/calculation

3.1. Phase filtering and ex vivo mouse brain image reconstruction

SWI and HCSF SWI reconstructed images were obtained by implementing algorithms in MATLAB® version R2013a running on a 12 core 64 GB 64-bit Windows 7® Dell Precision T7500 workstation. Specifically, the original MRI data are complex signals containing magnitude and phase information, which can be written as (Wang et al., 2000):

$$I(x, y, z) = M(x, y, z)\, e^{i\theta(x,y,z)}, \tag{1}$$

where I is the reconstructed complex signal for a voxel with coordinates (x, y, z), and M and θ are the magnitude and phase signals, respectively. In the *ex vivo* mouse brain study magnitude images were generated by taking the absolute value of Fourier-transformed k-space data. The voxel intensities were then normalized to the range [0, 1] for visualization purposes.

The application of low spatial frequency filtering of phase signals serves the purpose of removing unwanted background effects due to gradients and instrumentation. The amount of information retained or removed changes the extent to which phase signals due to sample susceptibility are retained. Hence, the filter cut-off affects the result. When the established method of homodyne filtering is used to remove low spatial frequency phase differences, the amount of high frequency information contained in the phase mask is a function of Fourier filter size. Previous results suggest that a Fourier filter size of at least 1/8th or larger of the image matrix size should be applied to remove background variations and unwanted phase information effectively (Barnes and Haacke, 2012; Rauscher et al., 2003; Wang et al., 2000). Several methods including polynomial fitting and projection onto dipole fields have been proposed for filtering of raw phases (Duyn et al., 2007a; Lee et al., 2013; Liu et al., 2011). These methods have been shown to improve the high-pass filtered phase result at air-material interfaces but not within the brain. As our work deals with the perception of image information within the brain, we limited our study to the application of homodyne filtering of raw signal phases.

To briefly explain homodyne filtering, we begin by noting that the Fourier filter is a symmetric low pass filter that removes high-frequency k-space content. The filtered complex signals (I_F) can be written as:

$$I_F = M_F e^{i\theta_F} \tag{2}$$

where M_F and θ_F are the low pass filtered magnitude and phase maps, respectively. The high frequency component of the phase is obtained by the division of the original image by the filtered complex image. This division of two complex images is termed homodyne

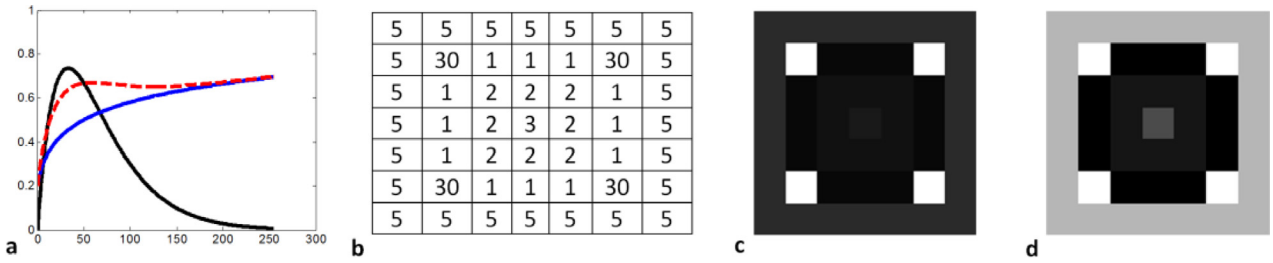

Fig. 1. Depicted is the (a) human contrast sensitivity as a function of spatial frequency. Illustration is arbitrary to highlight that the human visual system has low-sensitivity to high spatial frequencies (solid black line). Also plotted in (a) are the shape of the amplification function (solid blue line) and ideal sensitivity to spatial frequencies (dashed red line). In (b) an example 7 by 7 grid is shown having intensity values between 0 and 30. Correspondingly, (c) shows the image depicted directly and when (d) HCSF is used to amplify the spatial frequencies.

filtering:

$$\frac{I}{I_F} = \left(\frac{M}{M_F}\right) e^{i(\theta-\theta_F)} \tag{3}$$

where $\theta - \theta_F$ is the high frequency phase information (which comprises a high pass filtered phase map). In our study, the size of the Fourier filter was defined as $W_H \times W_H$, formed using the Hamming window function in MATLAB and applied in k-space. To evaluate the effect of applied filter size, it was varied between 32 (1/8th of the image matrix) and 256 (the size of the image matrix).

3.2. Combining band pass filtered phase images for HCSF SWI

In this study, phase images were combined by consecutively adding band pass filtered phase data obtained from the difference between two low pass filtered phase images written as:

$$P_{com} = H_L \times P_L + \sum_{l=1}^{L-1} H_l \times (P_l - P_{l+1}) \tag{4}$$

where P_{com} is the combined phase image, P_l are L high pass filtered phase images between $W_H = 32$ and $W_H = 256$ in predefined increments, and H_l are scalar valued weights obtained using the HCSF. Effectively, $P_l - P_{l+1}$ in Eq. (4) are individual consecutive band pass filtered phase images. In the case when all weights (H_l) equal to 1, the result is a sum of band-pass filtered phase images that ideally overlap such that when they are added the result is P_1 (i.e. the high-pass filtered phase as generated by the SWI sequence on the scanner). By increasing the values of H_l with increases in spatial frequency defined through the modified HCSF, we amplify the high-spatial frequency content. We tested a number of high-pass filters (Hann, Hamming, Blackman) to generate P_l and found that the Hamming window was able to best capture the original phase image when all H_l were set to 1. Therefore, this work is based on high-pass filtering of phase images using the Hamming-based windowing.

We evaluated separations of 8, 16 and 32, which are 1/32nd, 1/16th and 1/8th of the matrix size, to establish the impact of the band pass parameters on the SWI reconstructions. Moreover, the addition of the P_L term preserves high frequency content. In preliminary tests, we found that individual band-pass filters have to overlap by 1/8th of W_H on each side to be able to restore the original image by summing all band-pass images.

3.3. HCSF based phase mask

The human contrast sensitivity function defines the sensitivity of the human retina to the spatial frequencies in an image through the following equation (Farrell, 1999):

$$H(f) = k(bf)^a e^{-bf} \tag{5}$$

where f is the spatial frequency of an image, and k, a and b are parameters used to change sensitivity across the spatial frequency spectrum. In what follows, we set $k = 1$, since this value affects all values within the image without affecting contrast. Furthermore, in the discrete form of Eq. (5) we defined the lth band passed frequency as $H(f_l) = H_l$ for convenience. We changed $-b$ to b in Eq. (5) to obtain a modified HCSF , effectively amplifying high spatial frequency information. With a and b set for an image, the weights H_l were obtained and normalized to (0, 1] to be consistent with the range of values used in traditional SWI phase masks. The normalized values were then used in Eq. (4).

3.4. SWI reconstruction

The SWI reconstruction combines the magnitude and phase images in a voxel-by-voxel manner (Barnes and Haacke, 2012; Haacke et al., 2004b; Haacke et al., 2009; Robinson and Bhuta, 2011):

$$I_{SWI}(x, y, z) = M(x, y, z) \circ PM(x, y, z)^m \tag{6}$$

where o is the Hadamard product, I_{SWI} is the susceptibility-weighted image at voxel (x, y, z), M is the corresponding magnitude signal, and PM is the phase mask with filtered and masked phases in accordance with Haacke et al.'s original outline (Haacke et al., 2004a). m is the power used to change the distribution of values in PM. In our study, PM for the conventional SWI reconstruction was obtained with commonly used values for $W_H = 64$ and $m = 4$ (Barnes and Haacke, 2012; Haacke et al., 2007).

The negative phase values were set to zero and the positive values were mapped to (0, 1] to obtain both the SWI and modified HCSF SWI results (according to Haacke et al., 2004a either positive or negative phase values can be set to zero prior to mapping to (0, 1]). In the new method m was not used and PM was created using the modified HCSF function. Fig. 2 shows the steps involved in producing the modified HCSF SWI result. Essentially, band-pass filtered phase images ($P_l - P_{l+1}$ in Eq. (4)) were first computed, after which a new phase image (P_{com}) was obtained in which band-pass filtered phase images were amplified using H_l. Notably, our results cannot be achieved through histogram equalization. This is because histogram equalization emphasizes image content across all spatial frequencies of the image through re-binning, whereas we focus on emphasizing spatial frequencies where human contrast sensitivity is low irrespective of the spatial frequency distribution.

The creation of the phase mask in SWI involves four steps: (i) filtering of raw phase, (ii) truncation of positive or negative phases, (iii) conversion to the range (0, 1], and (iv) raising individual entries to a power to redistribute values in (0, 1]. For the modified HCSF SWI reconstruction steps (i) and (iv) are not needed, because the HCSF already has a high-pass filter component (see Fig. 1 wherein at low spatial frequencies the function goes to zero), and we do not use the raising to a power method (i.e. m) for redistribution of values, instead

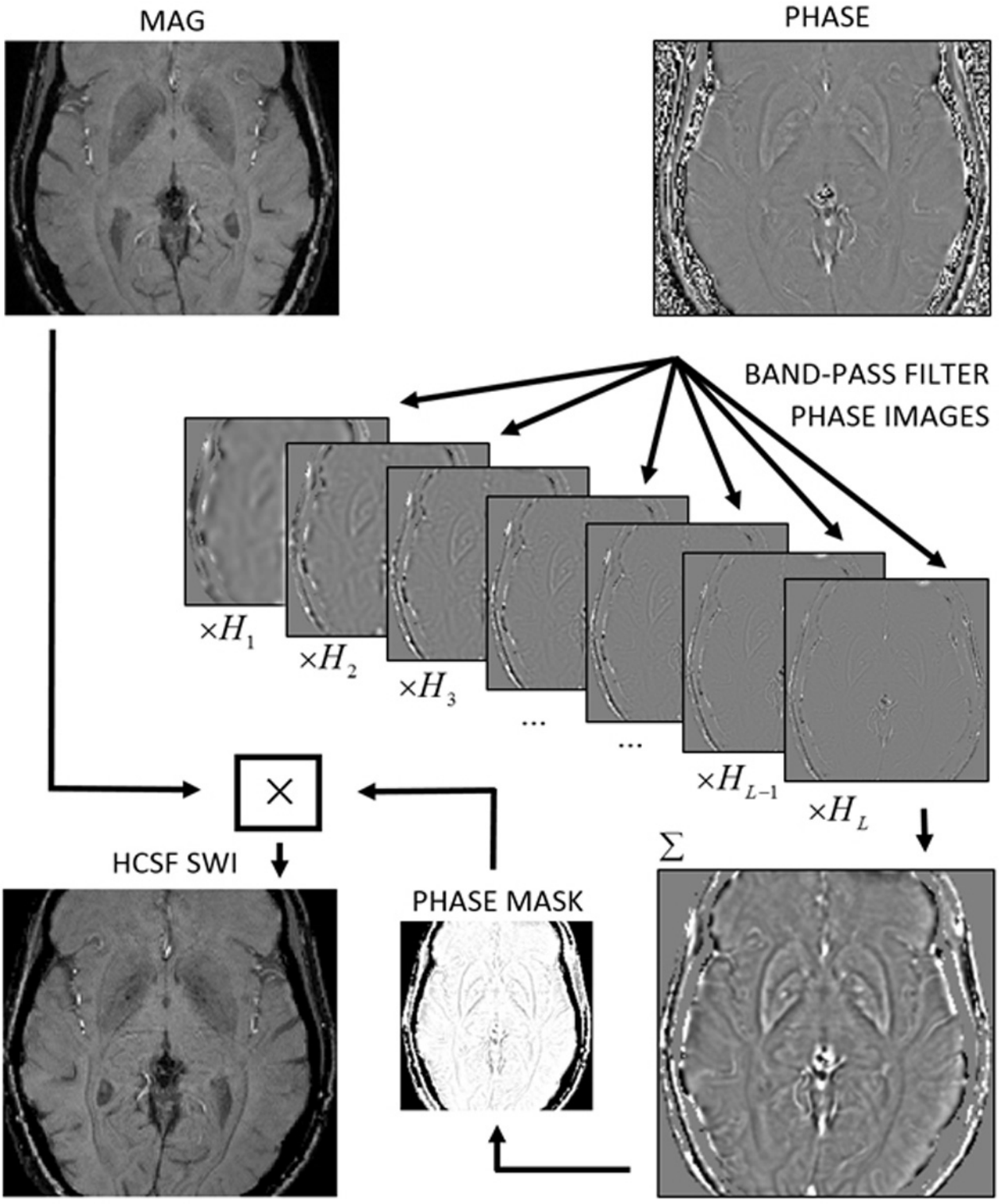

Fig. 2. Steps involved in producing the modified HCSF SWI result from acquired gradient recalled echo MRI magnitude (MAG) and phase (PHASE) images. The process of combining individually weighted (by H_1 to H_L) band-pass filtered phase images is governed by Eq. (4) and the weights are derived using Eq. (5). The marked increase in contrast in the combined phase image (Σ) is used to generate the phase mask applied as an entry-wise multiplication with the magnitude image to obtain the result.

we employ the modified HCSF. Hence, the modified HCSF is applied to raw phase, or to high-pass filtered phases generated by the SWI MRI sequence, after which entries are converted back to the range (0, 1]. This forms the mask applied to the magnitude image. For the *in vivo* human brain study the magnitude and phase images were used to create the HCSF SWI reconstruction. The magnitude and phase images used were ones produced by the available SWI sequence.

The magnitude and phase image produced by the SWI sequence of the scanner can be used to reconstruct the modified HCSF SWI result since the modified HCSF suppresses low spatial frequency content (see low-spatial frequency drop-off in Fig. 1). Furthermore, using the SWI sequence a high-pass filtered phase image is produced with consistent high-spatial frequency content when compared to the unfiltered phase image. Hence, the modified HCSF can be applied to either raw phases or already high-pass filtered phases generated by the scanner.

3.5. Qualitative and quantitative assessment of image quality

To determine the influence of parameter selection on the proposed method, parameter a was varied between 0.7 and 1.1 and parameter b was varied between 1 and 4. We selected one slice of the mouse brain image ($T_E = 8.5$ ms) for the first set of experiments.

After the parameters of the modified HCSF-based phase mask were determined, we applied the method to a single slice of the *ex vivo* mouse brain data set across the first six T_E acquisitions (3.5 ms, 8.5 ms, 13.5 ms, 18.5 ms, 23.5 ms, and 28.5 ms) and compared the results with the conventional SWI reconstruction qualitatively and quantitatively using image quality metrics.

Six image quality metrics were used to compare SWI reconstructions and HCSF-modified SWI. Three image similarity metrics were used to measure the preservation of information between traditional SWI and HCSF-modified SWI reconstructions: Cross Entropy, Correlation Coefficient and Mutual Information (Fazel et al., 2011). Specifically, if the intensities of the two images compared are considered as random variables, Cross Entropy describes the difference between the probability distribution functions estimated from the image histograms. Correlation Coefficient quantifies the degree of similarity between the two random variables as defined by their covariance and Standard Deviations. Mutual Information is regarded as the amount of uncertainty in one image that is reduced by knowing the other. Smaller values of Cross Entropy and larger values of Correlation Coefficient and Mutual Information indicate greater similarity between images. We also evaluated image quality using Intensity Entropy, the Mean Absolute Difference Coefficient, and the Standard Deviation of each image. Intensity Entropy represents the amount of visual information contained in the image; Mean Absolute Difference Coefficient is the mean of summated intensity differences between the rows and columns of the image; and Standard Deviation defines how much image intensities vary from the mean image intensity. The quantitative metrics used in this study have been widely applied for the comparison of medical images and for the assessment image content. Frequency spectrums were generated by Fourier transforming phase masks and plotting positive frequency values. The spectrums were analyzed qualitatively with the aim that large frequency values were sought to increase using the HCSF-modified SWI phase mask in comparison to the traditional SWI phase mask.

For qualitative evaluation, experts were asked to rate *in vivo* human brain images reconstructed using SWI and HCSF-modified SWI. Two separate data sets of 20 images from 5 patients were generated with individual images and reconstructions ordered randomly. Four expert raters (1 radiologist, 1 radiographer and 2 neuroscientists) rated all images in the data sets in two separate trials separated by an interval of 5 days. The images were rated between 1 (worst) and 5 (best) and results were tabulated prior to visual evaluation. The raters were instructed to try their best to keep the scoring consistent across all the images in one trial by studying all of the 160 images prior to rating them. The criterion for rating was appearance as determined by clarity and amount of detail contained within them. In total there were 320 scores for 20 images processed with 2 different methods and evaluated by 4 raters in 2 trials.

We also computed the power spectrum of each phase mask in each in-plane coordinate direction. We only provide power spectra from the vertical orientation, since the underlying trend was consistent irrespective of the direction chosen in the analysis.

3.6. Statistical analysis

Image quality metrics were compared using the paired t-test. The correlation between difference in image quality metrics and in image rating for the two reconstruction methods was assessed using Pearson's Correlation Coefficient. The difference in scores was calculated by subtracting the value for traditional SWI from that for HCSF-modified SWI. The paired t-test was employed for identifying statistically significant differences in the means of image quality metrics between SWI and HCSF-modified SWI. Repeated measures Analysis of Variance (ANOVA) was used to identify the contributions of inter- and intra-rater variability and of the different reconstruction methods to the total variance in the scores. To remove the main effect for rater and trial, the relative score difference was calculated as $(\text{Score}_{\text{HCSF}} - \text{Score}_{\text{SWI}}) / \text{Score}_{\text{SWI}}$. The cases were split into two groups: one with relative score difference larger than the median value and the other with the rest of the cases. To identify any significant differences, the mean values of the improvement in the three image quality metrics over the two groups were compared using t-test without the assumption of equal variances. Significance level of all hypothesis tests was 0.05.

4. Results

4.1. HCSF parameter selection

We investigated values for a and b over a broad range of values and provide results where meaningful changes were observed. The first set of results corresponds to a varying an in the range 0.7–1.1 when both k and b were set to 1. The conventional SWI and HCSF-modified SWI results when a is varied are provided in Fig. 3. To the right of each reconstructed image, respective phase mask spatial frequency (f in Eq. (5)) distributions are shown, and Table 1 quantifies the findings. The application of the HCSF phase mask evens out the spatial frequencies across the entire spectrum in comparison to traditional SWI; however, amplification of low spatial frequencies is still present across all values of a. The dentate gyrus (DG) and pyramidal cell layer (PCL) of the hippocampus (Paxinos and Franklin, 2003), for example, can be observed more clearly in the HCSF-modified SWI image than in the conventional SWI, as highlighted by the arrows in Fig. 3. When $a > 0.9$, Cross Entropy was found to decrease while Mutual Information increased, indicating that the difference between conventional SWI and HCSF-modified SWI decreased. Correlation Coefficient values varied only slightly with a. For values of $a < 0.6$ and >1.2 SWI and HCSF-modified SWI reconstructions were similar and differences were not visible on visual inspection. This finding is consistent with the trend in Cross Entropy, Correlation Coefficient and Mutual Information. Intensity Entropy, Mean Absolute Difference Coefficient, and Standard Deviation of conventional SWI are given in Table 1. Intensity Entropy values were all higher for HCSF-modified SWI than for conventional SWI with a maximum of 3.8022 when $a = 0.9$. Mean Absolute Difference Coefficient and Standard Deviation of the two approaches were similar. SWI and HCSF-modified SWI were most dissimilar for $a = 0.8$ (see highlighted values of Cross Entropy, Correlation Coefficient and Mutual Information in Table 1). The Intensity Entropy image quality measure was largest for $a = 0.9$. Based on these results, and noting

that for $a = 0.9$ the results of Cross Entropy, Correlation Coefficient and Mutual Information were only marginally different from those for $a = 0.8$, we set $a = 0.9$ in the following evaluations.

The influence of b in the interval 1–4 was examined for $a = 0.9$ and $k = 1$. The conventional SWI and HCSF-modified SWI images are provided in Fig. 4 with quantitative results listed in Table 2. As b increased, the dissimilarity between SWI and HCSF-modified SWI reconstructions increased and the image quality metrics Intensity Entropy, Mean Absolute Difference Coefficient and Standard Deviation also increased. Inspection of the images of Fig. 4 and assessment of the spatial frequency spectra revealed that although high frequencies are amplified, so was the level of noise, necessitating a compromise between noise amplification and detail enhancement. A value of $b = 3.0$ was chosen so as not to allow the amplitude of high spatial frequency components of the phase mask to exceed that of low spatial frequency components which are typically emphasized in traditional SWI reconstruction. The results of Table 3 confirm that the smaller the value of b, the more similar the HCSF-modified SWI reconstruction is to the traditional SWI reconstruction.

As the value of b increased, greater detail of brain substructures was visible in the HCSF-modified SWI image. Furthermore, the amplitude of the frequency spectrum also increased with higher b. Intensity Entropy, Mean Absolute Difference Coefficient and Standard Deviation for HCSF-modified SWI were higher than those for conventional SWI, and for both reconstructions these indices were higher for higher b. We found that the higher the value of b, the higher the Cross Entropy and lower the Correlation Coefficient and Mutual Information. Based on these metrics, we found an increase in b results in additional detail which is more easily perceived visually, increasing the differences between conventional SWI and HCSF-modified SWI. However, image artifacts at the center and blurring around the edges of tissue structures are observable when $b > 3$. This phenomenon may be because the band pass filtered phases were over-enhanced. Therefore, the selection of b should be such that image information is maximized while minimizing adverse effects such as blurring of edges. Although $b = 4$ provides the highest quantitative level of image information, visual quality of the HCSF-modified SWI image is lower. In light of this, and to ensure that the amplitude of high spatial frequencies does not exceed that of low spatial frequencies, a value of $b = 3$ was chosen. Table 3 also confirms that the smaller the value of b, the more similar the HCSF-modified SWI image is to traditional SWI reconstruction.

4.2. Choice of window size

We evaluated the influence of changing band pass separation [W_H in Eq. (4)]. The frequency spectra and quantitative findings for both reconstruction methods are compared in Fig. 5 and Table 3. We considered band pass filter separations smaller than 1/8th of the matrix size because at larger values, low spatial frequency influences such as those due to instrumentation and gradients become evident. The effect of increasing band pass separation was similar to increasing b. There was a uniform increase in amplitude across the phase mask frequency spectrum but at 1/8th of the matrix size, the maximum amplitude in the spectrum was still below the low spatial frequency amplitudes of traditional SWI. The highlighted values of Table 3 show that at 1/8th of the matrix size, the dissimilarity between traditional SWI and HCSF-modified SWI reconstructions is greatest and all image metrics are maximized.

In Fig. 5, a larger number of brain structures, such as the subiculum transition area, subrachial nucleus, temporal association cortex, polymorph layer of the dentate gyrus and alveus of the hippocampus, can be identified in HCSF-modified SWI using different band pass separation values compared to conventional SWI reconstructions. Tissue substructures and individual tissue outlines are more clearly visualized with HCSF-modified SWI reconstructed using a band pass separation of 1/8th of the matrix size compared to reconstructions with smaller separations. Of the different separations tested, 1/8th of the matrix size yielded the most uniform phase mask frequency spectrum. Intensity Entropy, Mean Absolute Difference Coefficient and Standard Deviation increased as band pass separation was decreased for HCSF-modified SWI. Values for these metrics were higher for HCSF-modified SWI than for conventional SWI (Table 3). The Cross Entropy, Correlation Coefficient and Mutual Information metrics show that a band pass separation of 1/8th of the matrix size maximizes the difference between HCSF-modified SWI and conventional SWI. The post-processing computational time also increased for smaller band pass separations without a measurable improvement in image quality.

4.3. Multiple echo time ex vivo mouse brain experiment

On the basis of the initial results, we fixed parameters of Eq. (5) to $a = 0.9$, $b = 3$ and $k = 1$, set W_H separation in Eq. (4) to 1/8th of the matrix size and reconstructed susceptibility-weighted images from GRE MRI data sets acquired at a range of echo times (T_E). The results are provided in Fig. 6 and Table 4. As T_E increased, SWI and HCSF-modified SWI became more similar on visual inspection (Fig. 6) and according to Cross Entropy, Correlation Coefficient and Mutual Information metrics (Table 4). Greater detail was visible on HCSF-modified SWI at shorter echo times in comparison to traditional SWI (Fig. 6). Shorter echo times may be used in HCSF-modified SWI to achieve comparable reconstructions to traditional SWI with longer echo times. Long echo times are disadvantaged by lower signal-to-noise ratio of the magnitude data. For HCSF-modified SWI, Intensity Entropy, Mean Absolute Difference Coefficient and Standard Deviation are larger for $T_E < 23.5$ ms than for longer echo times. Cross Entropy, Correlation Coefficient and Mutual Information confirm that the information content of both conventional and modified HCSF-modified SWI reconstructions increases as T_E increases. Furthermore, the reduction in Cross Entropy and the increase in Mutual Information with an increase in T_E imply that information is preserved between methods. These results suggest that HCSF-modified SWI depicts information consistent with conventional SWI, but over an enhanced visual spectrum.

4.4. Human brain experiment

Traditional SWI and HCSF-modified SWI reconstructions were obtained using $a = 0.9$, $b = 3$ and $k = 1$ and W_H of 1/8th of the matrix size. Three examples of the 20 pairs of images rated by four experts are provided in Fig. 7. Table 5 summarizes the image quality metrics obtained for the human brain data. The Intensity Entropy ($p < 0.01$) and Mean Absolute Difference Coefficient ($p < 0.01$) metrics were significantly higher for HCSF-modified SWI than for SWI but the Standard Deviation ($p = 0.1077$) did not differ significantly.

The number of cases with positive normalized score difference was 74 (92.5%) and 69 (86.3%) out of 80 for the two trials, respectively. Overall, the percentage with positive normalized score was 89.4%. There was no case with negative normalized score difference. The median of normalized score difference was found to be 0.333. There were 72 and 88 cases in the groups with normalized score difference above (Group A) and equal to or below (Group B) the median value, respectively. The mean values of Intensity Entropy, Mean Absolute Difference Coefficient and Standard Deviation were 0.0278, 0.0009 and 0.0004 for Group A and 0.0245, 0.0019, and 0.0014 for Group B. The mean value of the improvement in Intensity Entropy of Group A was significantly higher than that of Group B ($p = 0.0196$). However, the mean values of the improvement in the other two image quality metrics of Group A were significantly lower than those of Group B, with p values of 0.0092 and 0.0054.

Mean ($\pm$ Standard Deviation) rater scores for traditional SWI and HCSF-modified SWI were respectively 2.7 $\pm$ 0.6 and 4.0 $\pm$ 0.7 in Trial

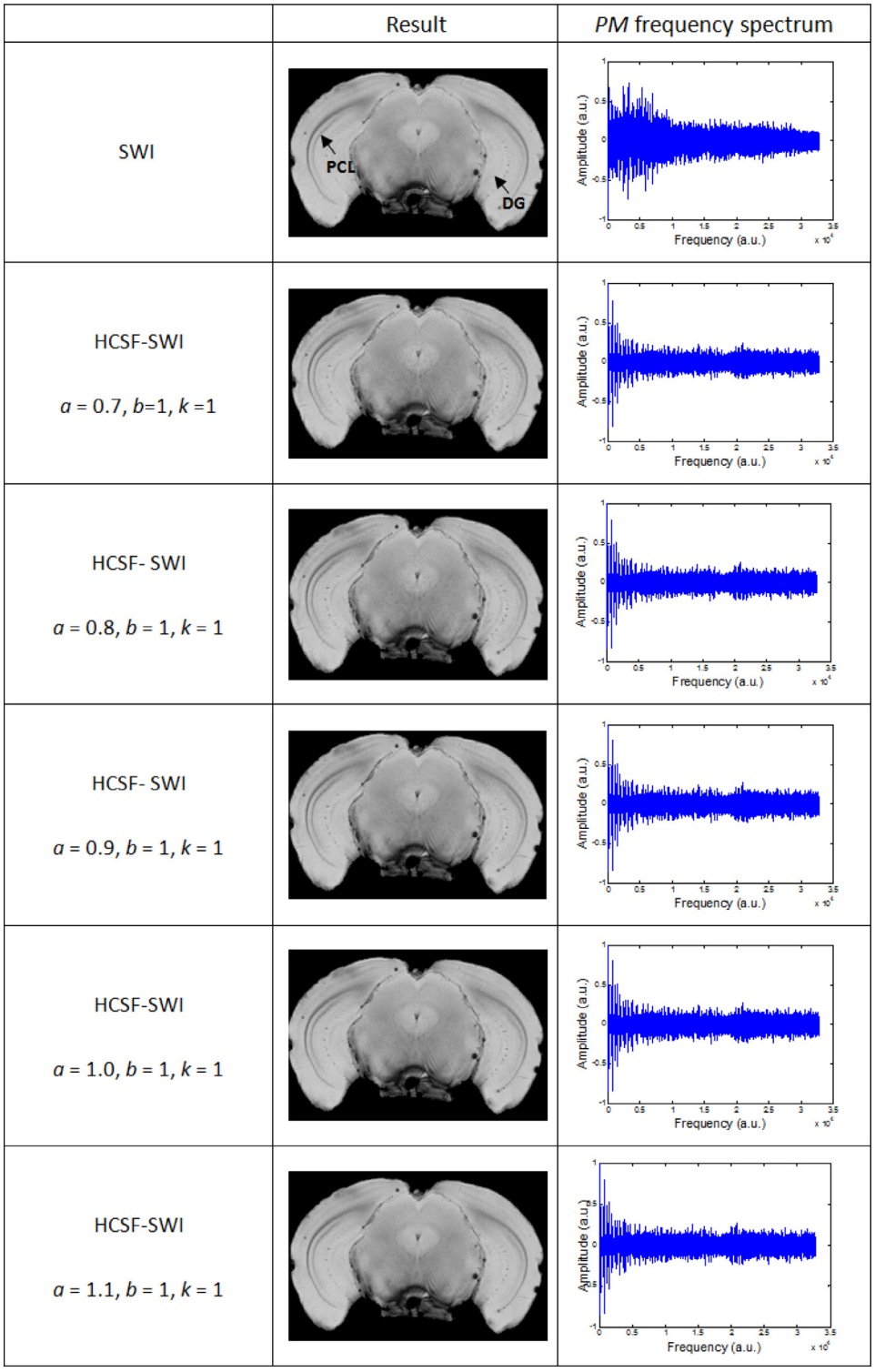

Fig. 3. Comparison of conventional SWI and modified HCSF-SWI when a is varied and b and k are kept constant. Along with the SWI reconstruction, the frequency spectrum of the phase mask used is also provided to show differences in the distribution of spatial frequencies. The following parameters were used: $b = 1$, $k = 1$, $W_H = (32, 64, 96, 128, 160, 192, 224, 256)$ corresponding to a separation of 1/8th of the matrix size, and $T_E = 8.5$ ms.

Table 1
Tabulated are image quality metrics corresponding to results provided in Fig. 3. Modified HCSF parameters b and k were fixed as 1.0 and 1.0, respectively. For CE, CC and MI, direction of arrow indicates increased level of similarity between SWI and HCSF SWI. An increase in Ent is associated with an increase in visual information, but increases in MADC and STD may not necessarily reflect increased level of information. We chose to set $a = 0.9$ based on these results and those depicted in Fig. 3.

	Image similarity metrics			Image metrics		
	CE↓	CC↑	MI↑	Ent↑	MADC	STD
SWI	–	–	–	3.7744	0.1045	0.1445
$a = 0.7$	0.0062	0.9987	1.4489	3.7894	0.1019	0.1386
$a = 0.8$	**0.0071**	**0.9983**	**1.4044**	3.8010	0.1037	0.1413
$a = 0.9$	0.0062	0.9982	1.4046	**3.8022**	**0.1047**	0.1429
$a = 1.0$	0.0046	0.9985	1.4351	3.7942	**0.1047**	**0.1432**
$a = 1.1$	0.0038	0.9989	1.4915	3.7828	0.1039	0.1422

Table 2
Tabulated are image quality metrics corresponding to results provided in Fig. 4. Modified HCSF parameters a and k were fixed as 0.9 and 1.0, respectively. For CE, CC and MI, direction of arrow indicates increased level of similarity between SWI and HCSF SWI. An increase in Ent is associated with an increase in visual information, but increases in MADC and STD may not necessarily reflect increased level of information. We chose to set $b = 3$ based on these results and those depicted in Fig. 4.

	Image similarity metrics			Image metrics		
	CE↓	CC↑	MI↑	Ent↑	MADC	STD
SWI	–	–	–	3.7744	0.1045	0.1445
$b = 1.0$	0.0062	0.9982	1.4046	3.8022	0.1047	0.1429
$b = 2.0$	0.0097	0.9966	1.3386	3.8221	0.1063	0.1444
$b = 3.0$	0.0136	0.9943	1.2945	3.8432	0.1091	0.1472
$b = 4.0$	0.0191	0.9911	1.2640	3.8667	0.1129	0.1510

Table 3
Tabulated are image quality metrics corresponding to results provided in Fig. 5. Fractions are with respect to image matrix size and HCSF parameters were $a = 0.9$, $b = 3.0$ and $k = 1.0$. For CE, CC and MI, direction of arrow indicates increased level of similarity between SWI and HCSF SWI. An increase in Ent is associated with an increase in visual information, but increases in MADC and STD may not necessarily reflect increased level of information. We chose to set $W_H = 1/8$th of the matrix size based on these results and those depicted in Fig. 5.

	Image similarity metrics			Image metrics		
	CE↓	CC↑	MI↑	Ent↑	MADC	STD
SWI	–	–	–	3.7744	0.1045	0.1445
1/32nd	0.0054	0.9983	1.4142	3.7977	0.1041	0.1421
1/16th	0.0082	0.9972	1.3585	3.8145	0.1055	0.1434
1/8th	**0.0136**	**0.9943**	**1.2945**	**3.8432**	**0.1091**	**0.1472**

Table 4
Tabulated are image quality metrics corresponding to results provided in Fig. 6. Values were obtained using a filter window separation of 1/8th of the image matrix, and HCSF parameters were $a = 0.9$, $b = 3.0$ and $k = 1.0$. For CE, CC and MI, direction of arrow indicates increased level of similarity between SWI and HCSF SWI. An increase in Ent is associated with an increase in visual information, but increases in MADC and STD may not necessarily reflect increased level of information. We found that for large echo times SWI and HCSF SWI converge to a similar result, and for smaller echo times HCSF SWI has superior contrast to traditional SWI at the same echo time.

		Image similarity metrics			Image metrics		
T_E	Reconstruction	CE↓	CC↑	MI↑	Ent↑	MADC	STD
3.5 ms	SWI	0.0140	0.9959	1.0902	3.5406	0.0773	0.1141
	HCSF SWI				3.6514	0.0842	0.1217
8.5 ms	SWI	0.0136	0.9943	1.2945	3.7744	0.1045	0.1445
	HCSF SWI				3.8432	0.1091	0.1472
13.5 ms	SWI	0.0111	0.9924	1.3433	3.9821	0.1392	0.1822
	HCSF SWI				4.0318	0.1435	0.1850
18.5 ms	SWI	0.0092	0.9916	1.3849	4.0644	0.1551	0.1957
	HCSF SWI				4.0947	0.1555	0.1947
23.5 ms	SWI	0.0097	0.9902	1.3677	4.1176	0.1672	0.2056
	HCSF SWI				4.1325	0.1640	0.2016
28.5 ms	SWI	0.0069	0.9892	1.4214	4.1697	0.1804	0.2184
	HCSF SWI				4.1757	0.1752	0.2129

Table 5
Mean and Standard Deviation of the image quality metrics across the 20 images.

Image metrics						Image similarity metrics		
SWI			HCSF SWI			SWI & HCSF SWI		
Ent	MADC	STD	Ent	MADC	STD	CE	CC	MI
.4764 ± 0.4040	0.1398 ± 0.0507	0.17 ± 0.0522	3.5024 ± 0.4030	0.1413 ± 0.0488	0.1709 ± 0.0501	0.0167 ± 0.0394	0.9981 ± 0.0003	1.3102 ± 0.1407

	Result	*PM* frequency spectrum
SWI	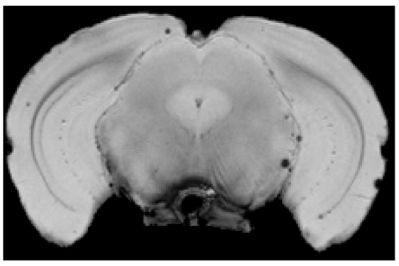	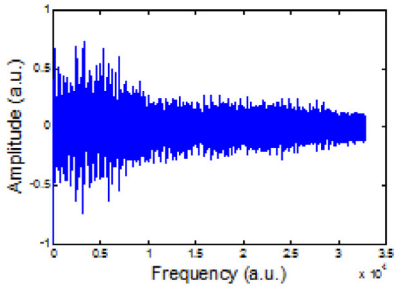
HCSF-SWI $a = 0.9, b = 1.0, k = 1$	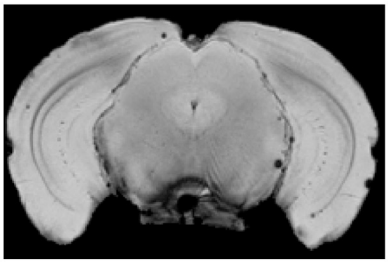	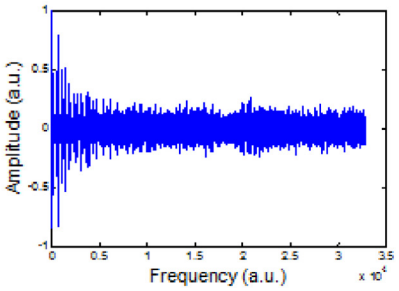
HCSF-SWI $a = 0.9, b = 2.0, k = 1$		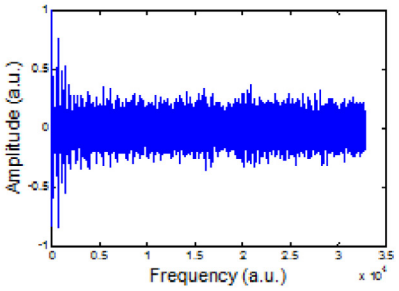
HCSF-SWI $a = 0.9, b = 3.0, k = 1$	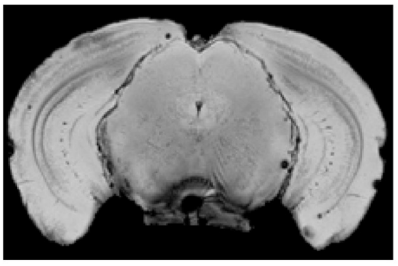	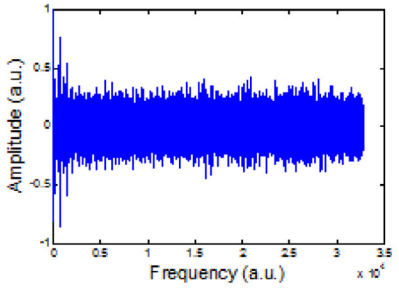
HCSF-SWI $a = 0.9, b = 4.0, k = 1$	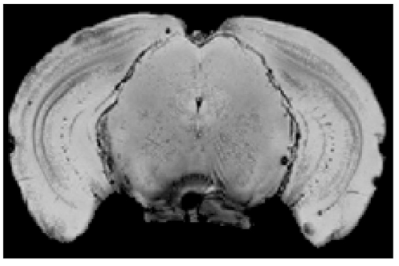	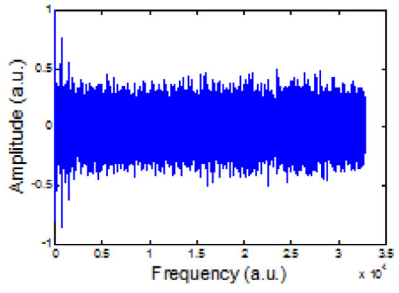

Fig. 4. Comparison of conventional SWI and modified HCSF-SWI when b is varied and a and k are kept constant. Along with the SWI reconstruction, the frequency spectrum of the phase mask used is also provided to show differences in the distribution of spatial frequencies. The following parameters were used: $a = 0.9$, $k = 1$, $W_H = (32, 64, 96, 128, 160, 192, 224, 256)$ corresponding to a separation of 1/8th of the matrix size, and $T_E = 8.5$ ms.

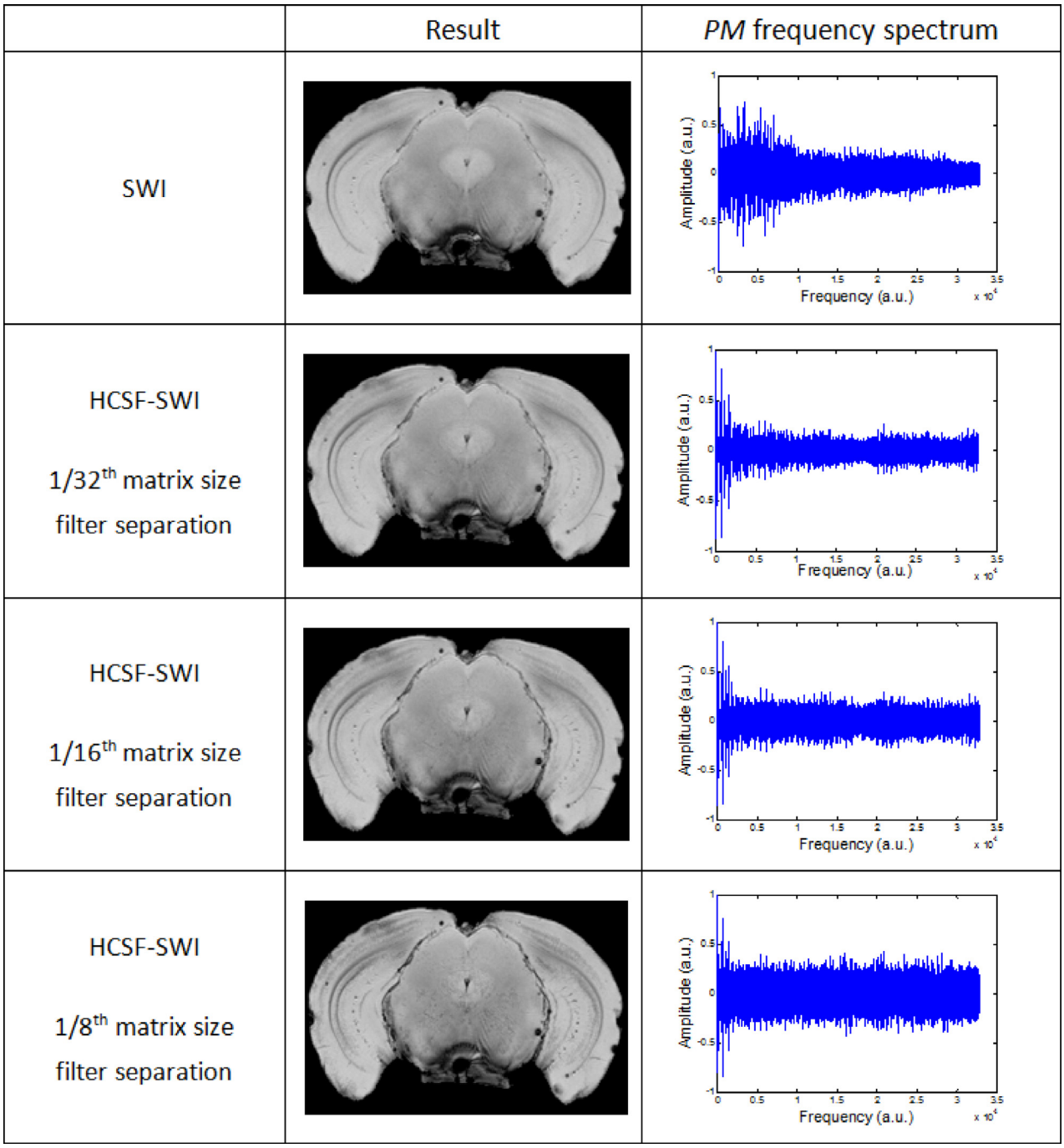

Fig. 5. Comparison of conventional SWI and modified HCSF-SWI when a, *b* and *k* are fixed and the filter separation is varied. Along with the SWI reconstruction, the frequency spectrum of the phase mask used is also provided to show differences in the distribution of spatial frequencies. The following parameters were used: $a = 0.9$, $b = 3.0$, $k = 1$ and $T_E = 8.5$ ms.

1 and 2.9 $\pm$ 0.7 and 3.9 $\pm$ 0.7 in Trial 2. A three-way ANOVA investigating the main effects of rater, trial, and reconstruction method and their interactions revealed a significant interaction between trial and method ($p = 0.02$). Two-way ANOVA for each trial showed no interaction between method and rater ($p = 0.7$ for Trial 1 and $p = 0.8$ for Trial 2). In both trials, the main effects of rater and method were significant ($p < 0.01$). The method and the rater respectively accounted for 52% and 9% of the total variance in Trial 1 and 36% and 16% of the total variance in Trial 2. For all raters, the score for HCSF-modified SWI images was equal to or greater than the score for SWI images.

In Fig. 7(a) regions around the putamen, claustrum and optic radiation of the HCSF-modified SWI reconstruction are enhanced with respect to traditional SWI. Furthermore, in Fig. 7(b) regions of globus pallidus and parahippocampal gyrus become perceivable using the HCSF approach, as indicated by arrows, while Fig. 7(c) depicts superior cortical structure near the precentral and postcentral gyrus and postcentral sulcus using the HCSF reconstruction. Fig. 7(d) shows a region of the cerebellum zoomed in and rotated clock-wise for visualization purposes. The secondary fissure and the lobules are particularly evident using the new reconstruction.

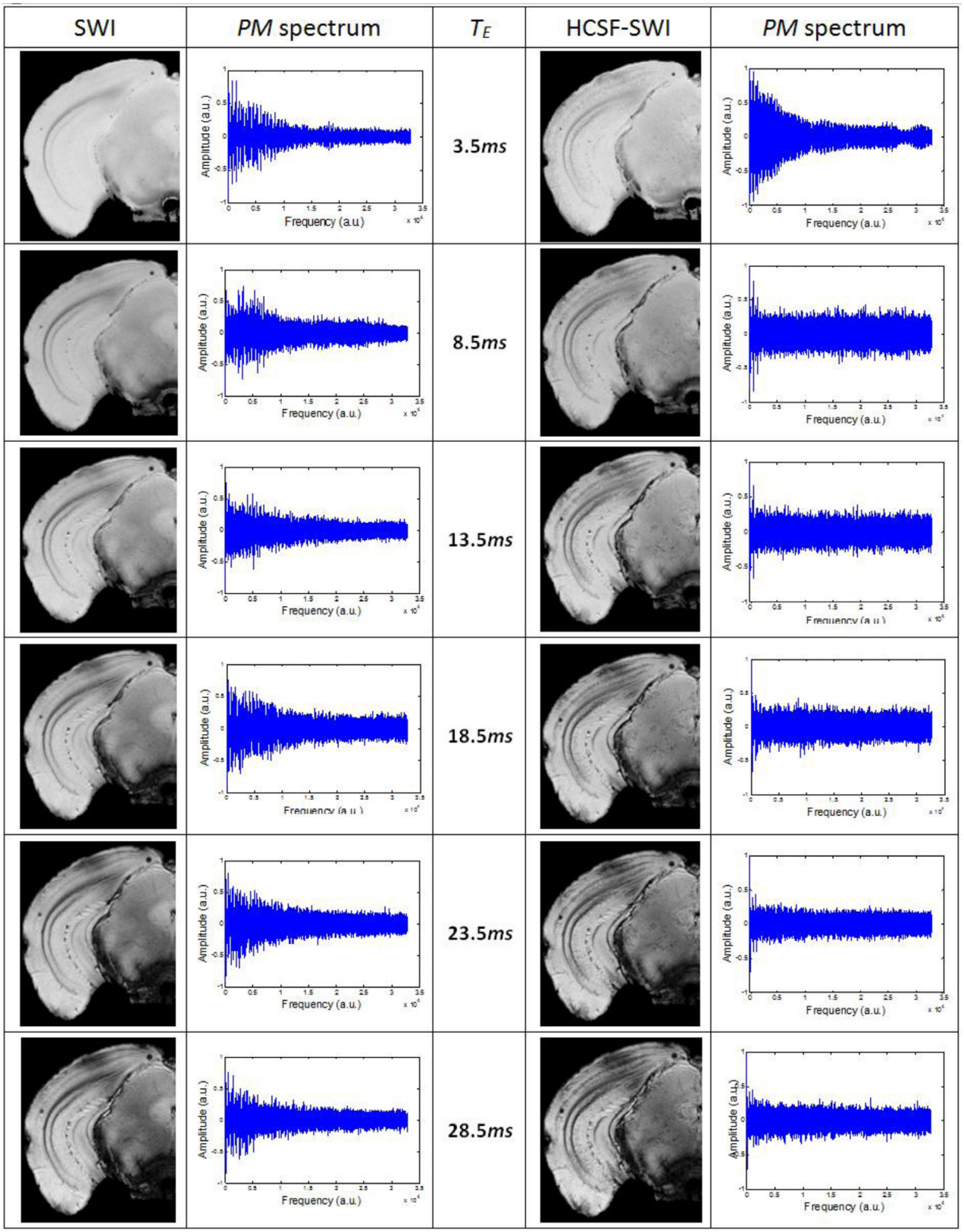

Fig. 6. Comparison of conventional SWI and modified HCSF-SWI when a, *b*, *k* and filter separation are fixed and T_E is varied. The following parameters were used: $a = 0.9$, $b = 3.0$, $k = 1$ and $W_H = (32, 64, 96, 128, 160, 192, 224, 256)$ corresponding to a separation of 1/8th of the matrix size.

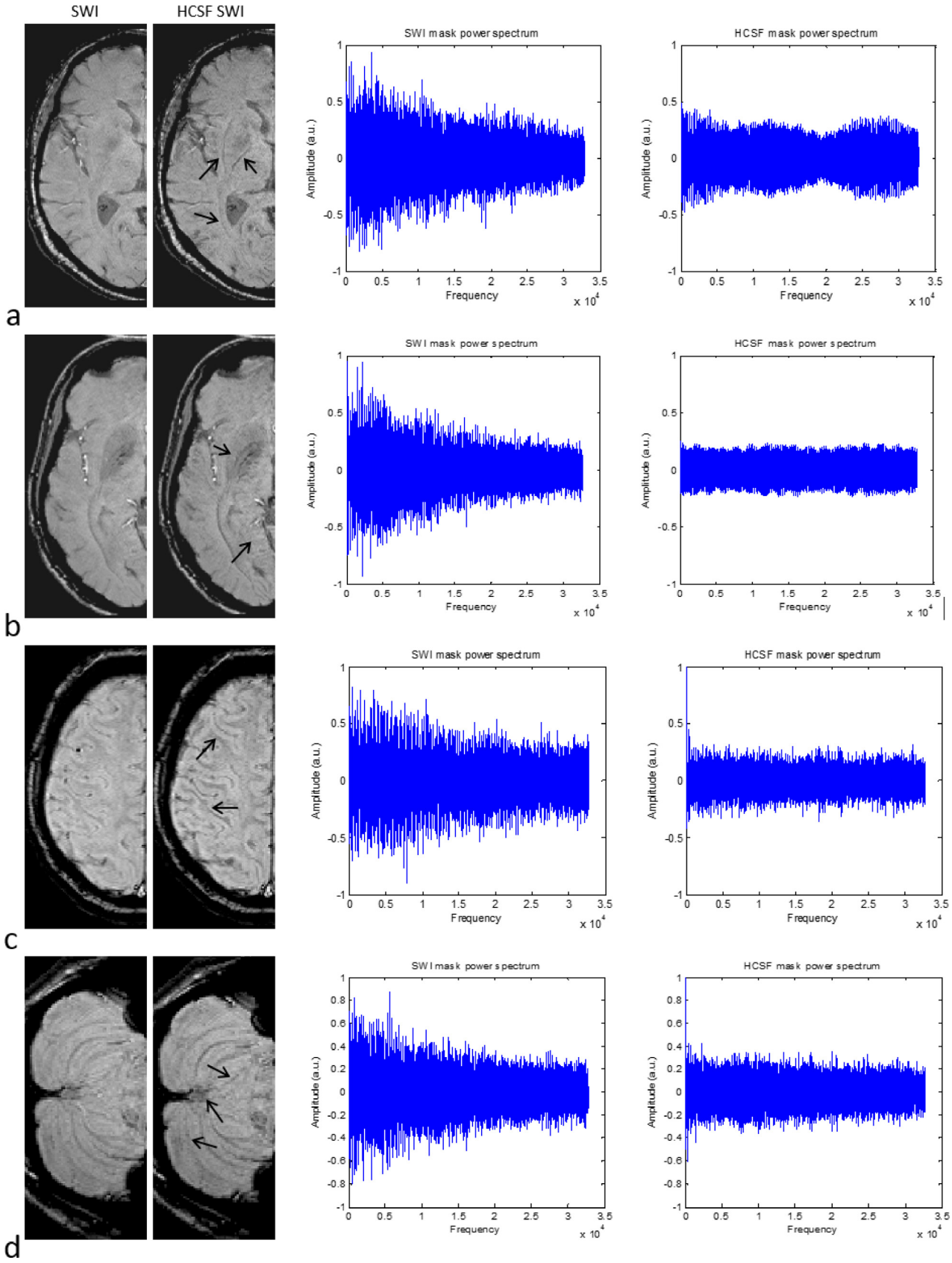

Fig. 7. Provided are three examples (a, b and c) of the SWI and HCSF SWI reconstructions used in the ratings. We also provide to the right corresponding power spectra of phase masks used in the reconstruction of the susceptibility weighted images. As shown by the arrows, regions around the putamen, claustrum and optic radiation are enhanced in (a) using the HCSF SWI approach. In (b) regions of globus pallidus and parahippocampal gyrus are qualitatively improved, and in (c) superior cortical structure is achieved near the precentral and postcentral gyrus and postcentral sulcus using the HCSF mask. In (d) the arrows (top to bottom) highlight improved contrast in the cerebellum around the secondary fissure, pyramis and uvula, and gracile lobule.

5. Discussion

The spatial frequency distribution in traditional SWI phase mask is manipulated by raising individual entries to a power with the goal of increased perception of information. Using the knowledge of the human contrast sensitivity function, we enhanced SWI phase masks by amplifying regions in the spatial frequency spectrum where sensitivity is low. Our results for an *ex vivo* mouse brain and *in vivo* human brains show that the HCSF-modified SWI can lead to images from which information is more easily perceived in comparison to the traditional SWI reconstruction.

Our perception of information is governed by the optical properties of the eye, the sampling aperture of cone photoreceptors and the properties of neurons with active and passive connections (Daly, 1992). Moreover, overall image size, eccentricity and level of background noise affect the way we perceive information contained in images. Models of visual perception are well established, and the human contrast sensitivity function links spatial frequency of images to our sensitivity of being able to notice corresponding information. Knowledge of sensitivity to spatial frequencies in images has been used to detect articles within scenes, track moving objects, increase specificity to recognition of, for example, faces, and classify image content (e.g. Papari et al., 2007; Richards et al., 1982). In this study, we aimed to amplify image content where sensitivity to spatial frequencies is low. To the best of our knowledge this is the first time the HCSF has been used in MRI.

SWI has become a routinely useful technique of depicting changes relating to cortical reorganization, iron deposition across the brain, arterial changes and plaques, stroke, and even myelination (Barnes and Haacke, 2012; Haacke et al., 2009; Lee et al., 2012; Meoded et al., 2013; Mittal et al., 2009). In view of the roll-off of contrast sensitivity with increasing spatial frequency (see Fig. 1(a)), we artificially enhanced SWI reconstructions by modifying the phase mask based on the HCSF. The result was improved perception of information contained in susceptibility-weighted images. We used image quality metrics to verify that information was preserved, and image perception was increased. Overall, our findings indicate that instead of raising the phase mask entries to a predefined power, as is the case traditionally, the technique based on the HCSF results in images of improved information perception. Such an approach of post-processing GRE-MRI acquired data can lead to improved qualitative assessment of images by radiologists and radiographers.

Based on qualitative results of Figs. 3–6 and quantitative results provided in Tables 1–4, we decided to set the band pass window size of 1/8th of the image matrix and $a = 0.9$, $b = 3.0$ and $k = 1.0$, which are parameters of the function used to enhance phase mask information. We found that a and b can selectively change the spatial frequency power spectra. In particular, a had a small effect, b had a large effect and multiple echo time reconstructions produced interesting results. Although an increase in b led to improved perception of high spatial frequency content in images, noise started to hinder images when b was larger than 3. Hence, we found a range of values for both a and b that maintained consistency of information while improving perception of image content. The significant increase in image Intensity Entropy of HCSF-modified SWI over traditional SWI finding implies that image improvements can be measured quantitatively using this metric. A significant difference was not found for the other metrics. In terms of varying the echo time of the data, we found that using the HCSF-based phase mask we could enhance short echo time GRE-MRI data to be equivalent to longer echo traditional SWI, where phase masks were raised to the power of 4. Thereby, already acquired GRE-MRI data with non-optimal choice of echo time, or GRE-MRI data that has heavy T_1-weighting and limited T_2^*-weighting, can be post-processed to create traditional SWI like reconstructions. This allows retrospective SWI studies to be conducted on GRE-MRI data initially collected for a different purpose.

Haacke et al. (2009) have outlined a number of applications for SWI. These include monitoring of iron in gray matter and calcification and micro-bleeds, all of which impact the phase image greatly due to the relative large local susceptibility effect. Local susceptibilities cause a local magnetic field change, which imprints on the phase image and the effect of which can be increased simply by increasing echo time. The use of long echo times for imaging large susceptibility effects can lead to locally extensive signal dephasing, which may result in localized signal loss in magnitude images. Because in SWI the magnitude image is the canvas on which the phase mask is applied, regions of low or zero signals cannot be enhanced through the application of the mask. Data collected with short echo times can therefore improve the canvas to which enhancement is applied, where the phase image is used to amplify information content of images across spatial frequencies of low human contrast sensitivity. Furthermore, in the presence of pathology that adds to the high spatial frequency content of images, it may be likely that the optimal values for a and b found here should be reassessed to maximize the benefits from qualitative assessment of images across applications.

The real and imaginary parts of the GRE-MRI data contain Gaussian noise, which in the magnitude image has been described as Rician noise and in the phase image the noise takes a more complicated form due to movement, breathing and pulsing of blood, and the action of the helium pump (Hagberg et al., 2012; Petridou et al., 2009). It is known, however, that noise in images is dominated by high frequency components. We showed qualitatively that using large values for b, not only the high spatial frequency content of the data was enhanced, but also noise started to hinder image quality. Quantitative assessment of the noise due to changes in b poses a new challenge, since in SWI both the magnitude and phase images play a role. Thereby, how noise in susceptibility enhanced images is evaluated has to be carefully considered. As future work, simulation studies focusing on specific applications and investigating how to best perform image enhancement using the human contrast sensitivity function should be performed.

The creation of the phase mask in traditional SWI involves a number of steps: high-pass filter raw phases, map filtered phases to masked values in (0, 1], raise the mask to a power (i.e. 4) and perform entry-wise multiplication of signal magnitude by phase mask. Our approach of using the HCSF-based mask modifies this pipeline in one way. That is, we do not raise the mask to a power. Instead, we use the knowledge of HCSF shape to amplify spatial frequencies where human contrast sensitivity is low. By binning spatial frequencies through the use of the band-pass filter (see Eq. (4)), we were able to selectively amplify regions across the spatial frequency spectrum. Our choice to employ band-pass filtering was based on the fact that in traditional SWI high-pass filtering is already performed, and by simply changing the cutoff of the high-pass filter, a band-pass response is achieved when two different cutoff frequency high-pass filtered data are subtracted. Therefore, algorithms already used in SWI can be applied to produce such results as those provided here.

6. Conclusion

We have developed an approach of creating phase masks to increase the perceivable level of contrast due to magnetic susceptibility in SWI. The use of the human contrast sensitivity function to enhance high spatial frequencies in a non-linear and non-conventional manner resulted in images having improved visual perception, as examined by image quality metrics and expert raters. In general, the HCSF-modified SWI result was better than that obtained for SWI in *ex vivo* mouse brain and *in vivo* human brain experiments. As SWI is used routinely within the clinic, the ability to increase perception of information contained in images plays an important role in imaging based diagnosis of diseases and disorders and patient care. In terms of pathology, brain diseases and disorders, which widely utilize SWI

to depict novel information about samples, further investigations are needed to realize the potential power of HCSF-modified SWI.

References

Barnes, S., Haacke, E.M., 2012. Susceptibility Weighted Imaging and MR Angiography. New York, NY.: Springer.

Beauchamp, M.H., Ditchfield, M., Babl, F.E., Kean, M., Catroppa, C., Yeates, K.O. et al, 2011. Detecting traumatic brain lesions in children: CT versus MRI versus susceptibility weighted imaging (SWI). Journal of Neurotrauma 28, 915–27. http://dx.doi.org/10.1089/neu.2010.1712, 21501069.

Daly, S.J., 1992. Visible differences predictor: an algorithm for the assessment of image fidelity. in: IS&T/SPIE's Symposium on Electronic Imaging: Science and Technology. International Society for Optics and Photonics, pp. 2–15.

de Champfleur, N.M., Langlois, C., Ankenbrandt, W.J., le Bars, E., Leroy, M.A., Duffau, H. et al, 2011. Magnetic resonance imaging evaluation of cerebral cavernous malformations with susceptibility-weighted imaging. Neurosurgery 68, 641–7, 21164377.

Deistung, A., Rauscher, A., Sedlacik, J., Stadler, J., Witoszynskyj, S., Reichenbach, J.R., 2008. Susceptibility weighted imaging at ultra high magnetic field strengths: theoretical considerations and experimental results. Magnetic Resonance in Medicine: Official Journal of the Society of Magnetic Resonance in Medicine / Society of Magnetic Resonance in Medicine 60, 1155–68. http://dx.doi.org/10.1002/mrm.21754, 18956467.

Duyn, J., van Gelderen, P., Li, T., de Zwart, J., Koretsky, A., Fukunaga, M., 2007. High-field MRI of brain cortical substructure based on signal phase. Proceedings of the National Academy of Sciences of the United States of America 104, 11796–801. http://dx.doi.org/10.1073/pnas.0610821104, 17586684.

Duyn, J.H., 2010. Study of brain anatomy with high-field MRI: recent progress. Magnetic Resonance Imaging 28, 1210–15. http://dx.doi.org/10.1016/j.mri.2010.02.007, 20392587.

Duyn, J.H., van Gelderen, P., Li, T.-Q., de Zwart, J.A., Koretsky, A.P., Fukunaga, M., 2007. High-field MRI of brain cortical substructure based on signal phase. Proceedings of the National Academy of Sciences of the United States of America 104, 11796–801. http://dx.doi.org/10.1073/pnas.0610821104, 17586684.

Farrell, J.E., 1999. Image quality evaluation, in: Macdonald, L.W., Luo, M.R. (Eds.), In Color Imaging: Vision and Technology. Wiley.

Fazel, S.A.A., Gal, Y., Yang, Z., Vegh, V., 2011. Qualitative and quantitative analysis of six image fusion methodologies and their application to medical imaging. in: International Conference on Digital Image Computing: Techniques and Applications. Queensland, Australia: Noosa.

Haacke, E., Mittal, S., Wu, Z., Neelavalli, J., Cheng, Y., 2009. Susceptibility-weighted imaging: technical aspects and clinical applications, part 1. AJNR. American Journal of Neuroradiology 30, 19–30, 19039041.

Haacke, E., Xu, Y., Cheng, Y., Reichenbach, J., 2004. Susceptibility weighted imaging (SWI). Magnetic Resonance in Medicine 52, 612–18. http://dx.doi.org/10.1002/mrm.20198.

Haacke, E.M., Kirsch, W., Ayaz, M., Khan, A., Manova, E.S., Krishnamurthy, B. et al, 2007. Establishing a baseline phase behavior in magnetic resonance imaging to determine normal vs. abnormal iron content in the brain. Journal of Magnetic Resonance Imaging: JMRI 26, 256–64. http://dx.doi.org/10.1002/jmri.22987, 17654738.

Haacke, E.M., Obenaus, A., Cheng, N.Y.C., House, M.J., Liu, Q., Neelavalli, J. et al, 2005. Imaging iron stores in the brain using magnetic resonance imaging. Magnetic Resonance Imaging 23, 1–25. http://dx.doi.org/10.1016/j.mri.2004.10.001, 15733784.

Haacke, E.M., Xu, Y., Cheng, Y.C.N., Reichenbach, J.R., 2004. Susceptibility weighted imaging (SWI). Magnetic Resonance in Medicine 52, 612–18. http://dx.doi.org/10.1002/mrm.20198.

Haacke, E.M., Ye, Y., 2012. The role of susceptibility weighted imaging in functional MRI. Neuroimage 62, 923–9. http://dx.doi.org/10.1016/j.neuroimage.2012.01.020, 22245649.

Hagberg, G.E., Bianciardi, M., Brainovich, V., Cassara, A.M., Maraviglia, B., 2012. Phase stability in fMRI time series: effect of noise regression, off-resonance correction and spatial filtering techniques. Neuroimage 59, 3748–61. http://dx.doi.org/10.1016/j.neuroimage.2011.10.095, 22079450.

Jagadeesan, B.D., Almandoz, J.E.D., Moran, C.J., Benzinger, T.L.S., 2011. Accuracy of susceptibility-weighted imaging for the detection of arteriovenous shunting in vascular malformations of the brain. Stroke; a Journal of Cerebral Circulation 42, 87–92. http://dx.doi.org/10.1161/STROKEAHA.110.584862, 21088245.

Kelly, D.H., 1975. Spatial frequency selectivity in the retina. Vision Research 15, 665–72. http://dx.doi.org/10.1016/0042-6989(75)90282-5, 1138482.

Lee, J., Shmueli, K., Kang, B.-T., Yao, B., Fukunaga, M., van Gelderen, P. et al, 2012. The contribution of myelin to magnetic susceptibility-weighted contrasts in high-field MRI of the brain. Neuroimage 59, 3967–75. http://dx.doi.org/10.1016/j.neuroimage.2011.10.076, 22056461.

Lee, Y., Han, Y., Park, H., 2013. A new susceptibility-weighted image reconstruction method for the reduction of background phase artifacts. Magnetic Resonance in Medicine.

Liu, T., Khalidov, I., de Rochefort, L., Spincemaille, P., Liu, J., Tsiouris, A.J. et al, 2011. A novel background field removal method for MRI using projection onto dipole fields (PDF). NMR in Biomedicine 24, 1129–36. http://dx.doi.org/10.1002/nbm.1670, 21387445.

Mannos, J., Sakrison, D., 1974. The effects of a visual fidelity criterion of the encoding of images. IEEE Transactions on Information Theory 20, 525–36. http://dx.doi.org/10.1109/TIT.1974.1055250.

Meoded, A., Poretti, A., Benson, J.E., Tekes, A., Huisman, T.A., 2013. Evaluation of the ischemic penumbra focusing on the venous drainage: the role of susceptibility weighted imaging (SWI) in pediatric ischemic cerebral stroke. Journal of Neuroradiology. Journal de Neuroradiologie.

Mittal, S., Wu, Z., Neelavalli, J., Haacke, E., 2009. Susceptibility-weighted imaging: technical aspects and clinical applications, part 2. AJNR. American Journal of Neuroradiology 30, 232–52, 19131406.

Papari, G., Campisi, P., Petkov, N., Neri, A., 2007. A biologically motivated multiresolution approach to contour detection. EURASIP Journal on Applied Signal Processing 2007, 119.

Paxinos, G., Franklin, K., 2003. The Mouse Brain in Stereotaxic Coordinates: Compact Second Edition. San Diego: Academic.

Petridou, N., Schäfer, A., Gowland, P., Bowtell, R., 2009. Phase vs. magnitude information in functional magnetic resonance imaging time series: toward understanding the noise. Magnetic Resonance Imaging 27, 1046–57. http://dx.doi.org/10.1016/j.mri.2009.02.006, 19369024.

Rauscher, A., Barth, M., Reichenbach, J.R., Stollberger, R., Moser, E., 2003. Automated unwrapping of MR phase images applied to BOLD MR-venography at 3 Tesla. Journal of Magnetic Resonance Imaging: JMRI 18, 175–80. http://dx.doi.org/10.1002/jmri.10346, 12884329.

Richards, W., Nishihara, H., Dawson, B., 1982. CARTOON: A Biologically Motivated Edge Detection Algorithm. Massachusetts Institute of Technology.

Robinson, R.J., Bhuta, S., 2011. Susceptibility-weighted imaging of the brain: current utility and potential applications. Journal of Neuroimaging: Official Journal of the American Society of Neuroimaging 21, e189–e204. http://dx.doi.org/10.1111/j.1552-6569.2010.00516.x, 21281380.

Vegh, V., Kording, F., Venkatachalam, T.K., Reutens, D.C., 2012. Magnetic susceptibility derived from T2 and T2*-weighted magnetic resonance magnitude images. Concepts in Magnetic Resonance Part B: Magnetic Resonance Engineering 41, 28–36.

Wang, Y., Yu, Y., Li, D., Bae, K.T., Brown, J.J., Lin, W. et al, 2000. Artery and vein separation using susceptibility-dependent phase in contrast-enhanced MRA. Journal of Magnetic Resonance Imaging: JMRI 12, 661–70. http://dx.doi.org/10.1002/1522-2586(200011)12:5<661::AID-JMRI2>3.0.CO;2-L, 11050635.

Zivadinov, R., Brown, M.H., Schirda, C.V., Poloni, G.U., Bergsland, N., Magnano, C.R. et al, 2012. Abnormal subcortical deep-gray matter susceptibility-weighted imaging filtered phase measurements in patients with multiple sclerosis: a case–control study. Neuroimage 59, 331–9. http://dx.doi.org/10.1016/j.neuroimage.2011.07.045, 21820063.